Engineering Geology 294 (2021) 106407

Contents lists available at ScienceDirect

Engineering Geology

journal homepage: www.elsevier.com/locate/enggeo

Deep void detection with 3D full waveform inversion of surface-based and in-depth source seismic wavefields

Majid Mirzanejad [a], Khiem T. Tran [a,*], Michael McVay [a], David Horhota [b], Scott J. Wasman [a]

[a] University of Florida, Department of Civil and Coastal Engineering, 365 Weil Hall, P.O. Box 116580, Gainesville, FL 32611, USA
[b] Florida Department of Transportation, 5007 N.E. 39th Avenue Gainesville, FL 32609, USA

ARTICLE INFO

Keywords:
Sinkhole
3D-FWI
SPT
Seismic
Deep voids

ABSTRACT

Detection of subsurface voids using nondestructive seismic methods is an ongoing problem in many areas of civil and environmental engineering (e.g., sinkholes and caves), homeland security (e.g., tunnel detection), and mining applications (e.g., abandoned mines). Recent advances in 3D full waveform inversion (FWI) technology have made it possible to scan large volumes of the underlying materials efficiently, providing a glimpse into the state of subsurface conditions. A challenge in applying 3D FWI methods to the detection of voids emerges from their embedment depths. Shallower voids are easier to detect due to their large signature on the surface seismic response, whereas deeper voids have a much smaller signature and are therefore much harder to detect. This is not a limitation of the FWI method, but rather that of the seismic field-testing techniques and data gathering processes. The goal of this study is to investigate ways to overcome these limitations and improve void detection depths. One way to achieve this is through the application of a large surface source, generating more energy at lower frequencies (longer wavelengths), thereby increasing the penetration depth. Another way is by increasing the contribution of body waves and utilizing the diffraction/transmission information embedded in the waveforms. The latter is achieved through the application of a recently developed SPT-seismic method, where the standard penetration test (SPT) device is used to generate wave motion from within the subsurface. Both source methods and a newly developed 3D Gauss-Newton FWI method are utilized here to detect a deep void (25–45 m depth) in limestone, on the southern peninsula of Florida. The results are compared with SPT and Sonar profiles obtained from the test site. Overall, a good image of the deep void is achieved, matching observations from the invasive results. The findings provide useful insight into the application of FWI technology for detecting deep subsurface voids and anomalies that are typically hard to identify.

1. Introduction

Successful detection of underground voids is crucial for design and construction of infrastructure (building, bridge, tunnel, etc.). If undetected, they can cause problems during construction operations, prolonging construction timelines, and increase costs for remediation and maintenance. Invasive testing at a construction site often fails to identify voids due to the limited soil volume that is examined. Invasive tests like the Standard Penetration Test (SPT) or the Cone Penetration Test (CPT) often end at less than 20-m depth, and as a result, voids at deeper depths are not identified. Deep and large voids, such as one presented in this study, may lead to excessive structural settlements or collapse manifested through massive sinkholes, resulting in significant property damage and even fatalities (Gutiérrez, 2016).

Noninvasive seismic methods provide an alternative solution and can be used in tandem with invasive testing to reduce the uncertainty in subsurface site characterization. The success of any void detection effort is dependent on multiple variables ranging from the size and depth of the void to the properties of the seismic source and testing configuration. Many seismic techniques have been developed and used in void detection with varying degrees of success. Surface wave-based methods, such as attenuation analysis of Rayleigh waves (Nasseri-Moghaddam et al., 2005; Putnam et al., 2009), multichannel analysis of surface waves (Park et al., 1999; Nasseri-Moghaddam et al., 2007), and backscatter analysis of surface waves (Sloan et al., 2012; Ivanov et al., 2017), have shown good potential in detecting shallow (<10 m) subsurface

* Corresponding author.
E-mail addresses: m.mirzanejad@ufl.edu (M. Mirzanejad), ttk@ufl.edu (K.T. Tran), mcm@ce.ufl.edu (M. McVay), david.horhota@dot.state.fl.us (D. Horhota), scott.wasman@essie.ufl.edu (S.J. Wasman).

https://doi.org/10.1016/j.enggeo.2021.106407
Received 27 April 2021; Received in revised form 23 September 2021; Accepted 3 October 2021
Available online 5 October 2021

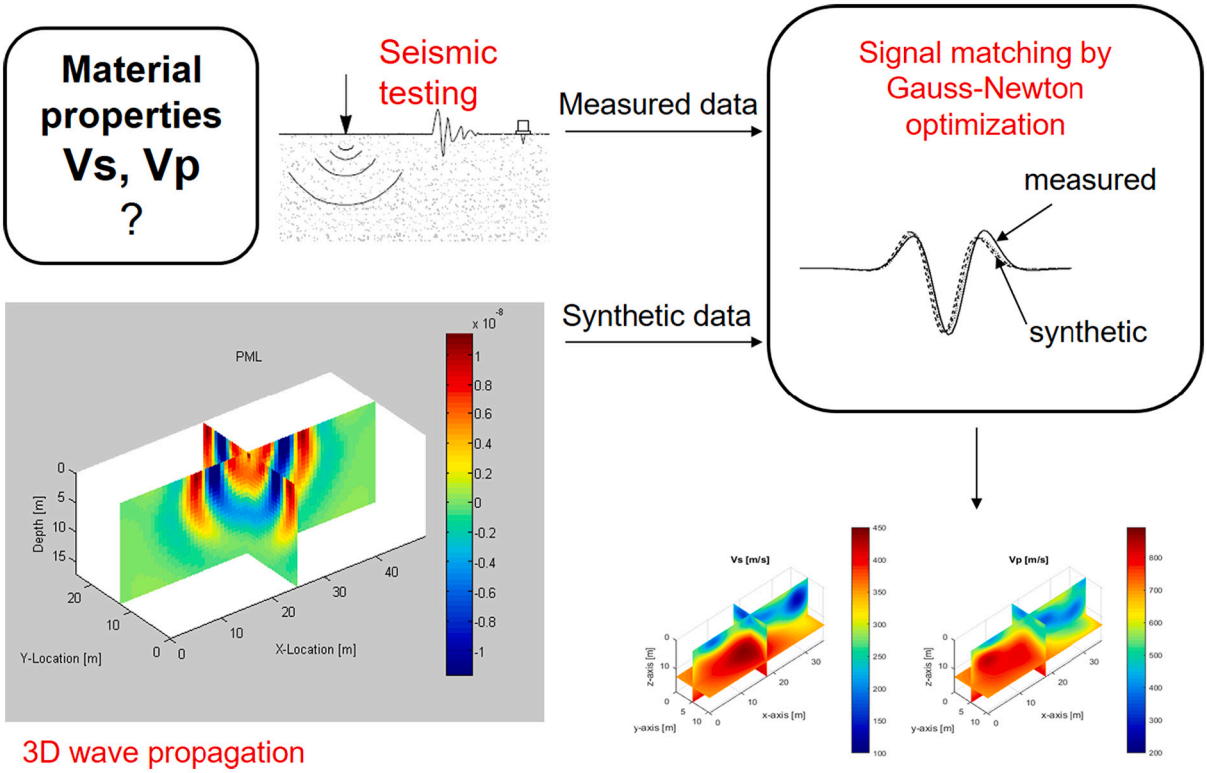

Fig. 1. 3D Full waveform inversion implementation.

anomalies (i.e., voids, pockets of soft deposits or loose materials, embedded objects). These methods, however, only utilize part of the properties of the seismic response (Vireux and Operto, 2009), limiting the characterized resolution and accuracy with depth.

Full waveform inversion (FWI) methods (Warner et al., 2013; Fathi et al., 2016; Nguyen and Tran, 2018; Köhn et al., 2019; Tran et al., 2019; Mirzanejad and Tran, 2019) utilize the full seismic response, which is rich in the spectral data as a result of energy transmission through geologic materials. Recent application of the surface-based 2D FWI (Romdhane et al., 2011; Tran et al., 2013; Groos et al., 2017; Wang et al., 2019; Kiernan et al., 2021) and 3D FWI (Plessix et al., 2010; Nguyen and Tran, 2018; Smith et al., 2019; Mirzanejad et al., 2020a) techniques has shown their capabilities in detecting shallow (<10 m) subsurface voids. This is due to the large signature of the shallow voids on the surface seismic response. Deeper voids have a much weaker effect, making them harder to detect and characterize (Sloan, 2017; Mecking et al., 2021).

A recent study by Mirzanejad et al., 2020b has shown that coupling the SPT and FWI method (SPT-seismic approach) can extend the void detection depths in situations with limited access on the surface. The mechanical energy generated during the driving of the SPT spoon into the subsurface has multiple advantages for seismic field investigations: 1) the body wave contributions to the waveform are increased, 2) illumination angles are not restricted as is the case of surface-based sources (Prada et al., 2000), and 3) the diffraction/transmission effects can be captured. In the study by Mirzanejad et al. (2020b), a 2D receiver array was placed on the ground surface to record the SPT-seismic response. A surface-based source was also used with the same receiver configuration, and the result was compared with that of the SPT-seismic approach. The surface-based method could not detect the deep void, while the SPT-seismic approach could detect the void and characterize its shape and embedment depth. The surface seismic source used in that study was a 40-kg drop weight propelled energy generator (PEG) with limited energy at low frequencies (<10 Hz). Using a heavier source with a larger impact area is expected to create greater energies at the lower frequency range (larger wavelengths) and should therefore increase the void detection depth.

This study was designed to test the hypothesis that more energy at low frequencies (<10 Hz) can detect deeper voids using surface-based testing, and to further examine the capabilities of the novel SPT-seismic approach in deep void detection (Mirzanejad et al., 2020b). A high energy source of 340-kg drop weight was used at a site on the southern peninsula of Florida, where a known deep void (25–45 m depth) exists. The limestone bedrock in this area is known to have many karst conduits at various scales that include voids on the order of several meters (Manda and Gross, 2006) to tens of meters. For the SPT-seismic testing, SPTs were performed at two locations adjacent to the void, not physically intersecting the void, to see if it could be detected while not physically identified by the SPT. The results from the analysis were compared to SPT data and borehole sonar imaging.

2. Methodology and implementation

The 3D FWI method (Tran et al., 2019) is used in this study. It utilizes an elastic finite difference forward solver to simulate wave propagation and Gauss-Newton method for model updating. The general concept of the FWI method is shown in Fig. 1 and the overall process is shown in the flowchart of Fig. 2.

For the model updating to extract material properties (S-wave and P-wave velocities, Vs and Vp), Gauss-Newton method matches the simulated (estimated) and field data by iteratively minimizing the least-squares error defined as:

$$E(\mathbf{m}) = \frac{1}{2}\Delta\mathbf{d}^t\Delta\mathbf{d} = \frac{1}{2}[\mathbf{F}(\mathbf{m}) - \mathbf{d}]^t[\mathbf{F}(\mathbf{m}) - \mathbf{d}], \quad (1)$$

where $\Delta\mathbf{d}$ is the waveform residual between the estimated waveform data $\mathbf{F}(\mathbf{m})$ from the forward simulation and field data $\mathbf{d}$. Parameter $\mathbf{m}$ denotes model parameter and holds Vs and Vp of all the cells, and t denotes the vector or matrix transpose.

At the start of each inversion iteration, the source signature is

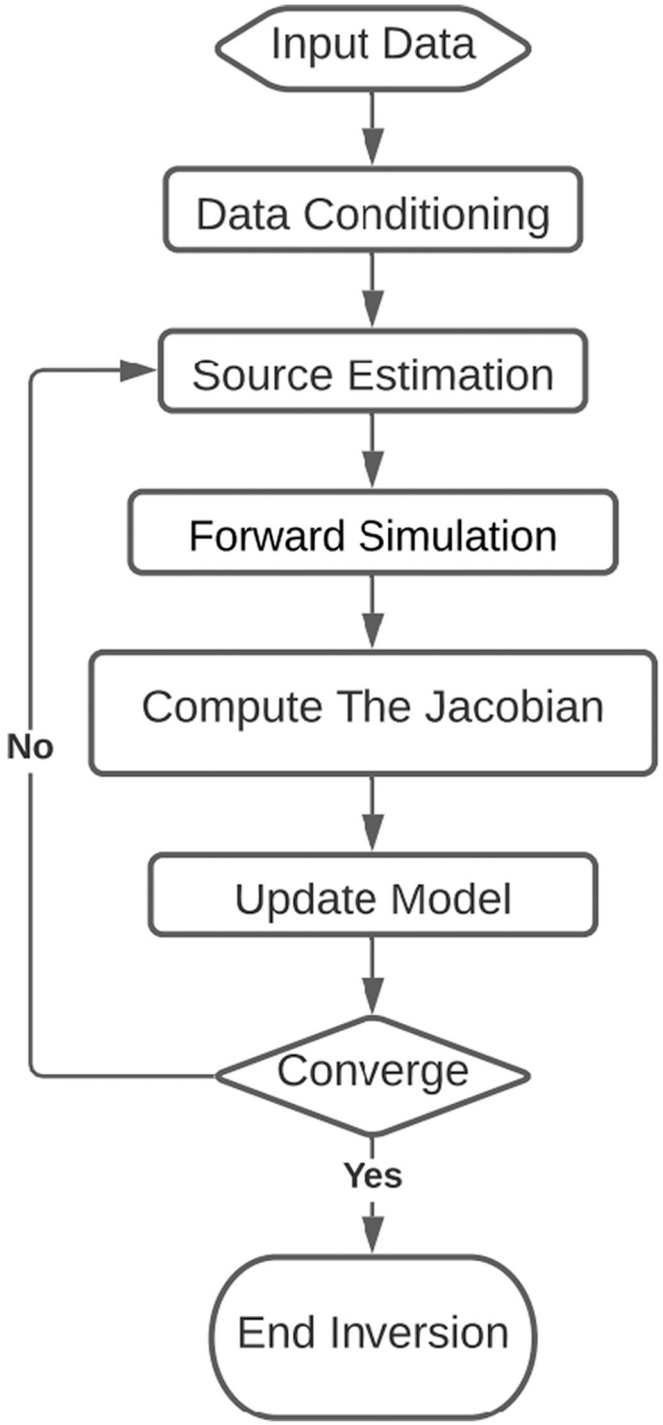

Fig. 2. Method implementation flowchart.

estimated from the collected field data. The source estimation is based on the deconvolution of the field seismic response with the Green's function obtained from the forward simulation. See Tran and Luke (2017) for more detail. The estimated source is then used for the forward simulation to compute the estimated waveform data **F**(**m**). Amplitude correction is then performed to account for the drop created in waveform amplitude from the intrinsic attenuation of the anelastic material. The estimated waveform data is adjusted by a correction factor of the form $y(r) = Ar^{\alpha}$ before matching with the field data, where r is the source-receiver distance, and factors A and α are determined in an iterative least-squares inversion process to minimize the energy of the waveform residuals. The factors A and α are updated at the beginning of each iteration. The correction via y(r) is used to account for intrinsic attenuation effects.

At the end of each iteration, the model parameter is updated using the following equation:

$$\mathbf{m}^{n+1} = \mathbf{m}^{n} - \alpha^{n}[\mathbf{J}^{t}\mathbf{J} + \lambda_1\mathbf{P}^{t}\mathbf{P} + \lambda_2\mathbf{I}^{t}\mathbf{I}\,]^{-1}\,\mathbf{J}^{t}\Delta\mathbf{d}, \quad (2)$$

where **J** is the Jacobian matrix, α^n is the step length at the current iteration n, which is equal to 1 for Gauss-Newton method. **P** is a matrix representing the 3D Laplacian operator that is used for regularization, and **I** is the identity matrix used to increase invertibility of the inverse Hessian matrix ($\mathbf{H_a} = \mathbf{J}^{t}\mathbf{J}$). Parameter λ_1 determines the degree of regularization used during the analysis. Larger values of λ_1 provides more regularization and a smoother image. Inversely, lower values of λ_1 provides less regularization and a sharper image. Parameter λ_2 denotes the degree of closeness to the Gauss-Newton method. Lower values for λ_2 means the updates follow Gauss-Newton method. Higher values for λ_2 means that the updates are more like the pure gradient descent method. These two parameters (λ_1, λ_2) are determined via trial-and-error to provide the best results, and for this study were determined as 0.02 and 0.0005 times of the maximum element values of $\mathbf{J}^{t}\mathbf{J}$ for λ_1 and λ_2, respectively. See Tran et al., 2019 for a detailed information of the mathematical formalism including the Jacobian calculation, model update, and parameter selection.

3. Surface-based source

3.1. Test site and field testing

The test site is on the southern peninsula of Florida with a known deep and large void identified from invasive SPTs. The borehole logs from the site revealed the existence of a shallow layer of dark organic fine to medium sand underlain by limestone of various types. Surface-based testing was first carried out using a large surface source shown in Fig. 3. The source weighted 340 kg, was dropped from a height of 45 cm, and had an impact area of 0.16 m^2. The system operated through a remotely controlled device raising and dropping the weight consistently each time, hitting the ground directly on impact. The test area was covered by embankments in the lateral direction facing north-south, and hence test lines were placed in the east-west direction. Based on available information from the SPTs, a part of the void was expected to be inaccessible because it was located underneath the two embankments located north and south of the testing zone. This may not be problematic, as seismic waves can penetrate outside of the testing area and detect adjacent anomalies.

Given the available information of void location and the two obstructing embankments, 72 geophones were placed in a 4 × 18 grid with a grid spacing of 3 m × 4.5 m, respectively (Fig. 4). The whole test area spanned 9 m in the north-south, and 76.5 m in the east-west directions. A grid of sources comprising of 46 shots were located and marked in the testing area. The shots were placed in the east-west direction at 4.5 m spacing, and in the north-south direction at 3 m spacing. The staggered grid configuration shown in Fig. 4 was chosen to facilitate source positioning, and to reduce source-receiver coupling.

Based on the above testing setup, the source (Fig. 3) was moved to the desired location for each shot and dropped under the force of gravity with the weight impacting the ground surface directly. The induced ground motion was picked up by the 72 geophones and recorded. Note that the pulse generated through the act of dropping the weight contains a wide range of frequencies, and as a result, needed to be filtered using a trapezoidal filter (Jordanov and Knoll, 1994) before the actual FWI analysis. The sampling rate of the seismographs was 0.5 ms for all recorded wavefields, and data was recorded for a duration of 1 s. This sampling rate allows frequencies as high as 1000 Hz to be accurately sampled (Nyquist frequency) without aliasing. Note that the frequency

Fig. 3. Florida test site: Large surface source used to generate seismic waves.

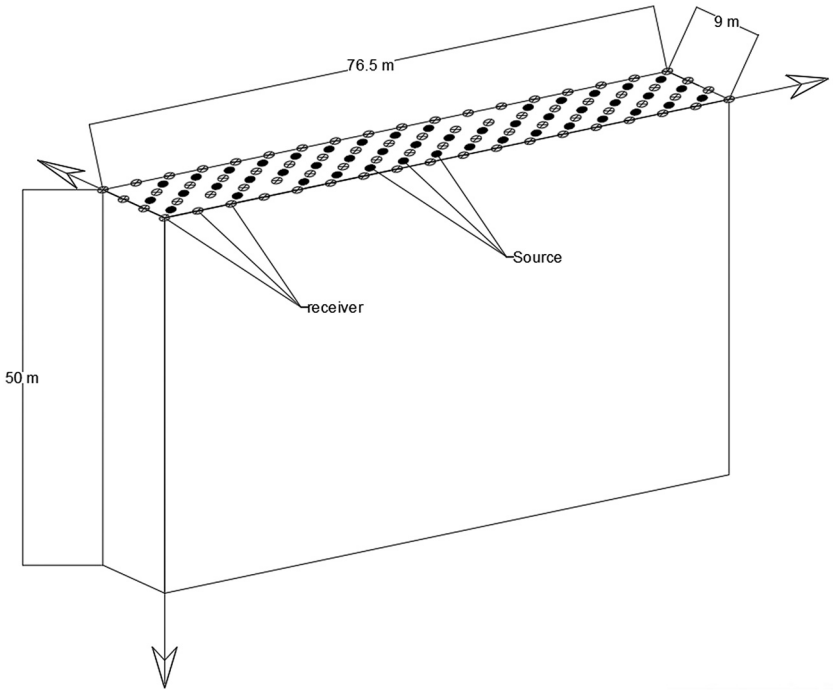

Fig. 4. Testing configuration used for surface-based analysis.

content of recorded data is mostly controlled by the source, not the sampling rate. The recorded data with consistent wave magnitudes and phases at most of receivers are in the range of 5–25 Hz, which were used for analysis.

3.2. Analysis and results

The size of the analyzed medium was 50 m × 85.5 m × 15 m (depth × length × width). As noted, the medium size was chosen to be larger than the testing size shown in Fig. 4 to capture the void image that lied outside of the testing area underneath the embankments. The embankments to the north and south as shown in Fig. 3 were not modelled in the forward solver for simplicity. A grid spacing of 1.5 m × 1.125 m × 1.5 m (depth × length × width) was used to facilitate the source and receiver placement on the numerical grid. Based on the spectral analysis of the recorded wavefields, a homogenous initial velocity of 400 m/s for Vs, and twice that for Vp was chosen for the starting point of the analysis (Fig. 5a).

The analysis began with the data filtered for the frequency window of 5–15 Hz, with a center frequency of 12 Hz, and ran for 5 iterations in the first stage. Receivers close to the source location (6 m radius) were removed from the analysis to reduce source-receiver coupling. The error decreased from a normalized value of 1 at the start of the inversion to 0.98 at the end of the first stage (Fig. 6). The results of the first inversion stage were then used as input to the second stage using a center frequency of 20 Hz, and a frequency window of 5–25 Hz. The stopping criteria was when the error did not decrease by more than 1% from its previous iteration for both inversion stages. The error decreased to a normalized value of 0.65 at the end of the inversion (Fig. 6). Note that the first stage was run at lower number of iterations to reveal larger features and make the velocity model ready for the second run. This staged frequency inversion allowed using a simple homogeneous initial model to achieve convergence, as lower frequencies (larger wavelengths) require less detailed initial models. Shown in Fig. 7 is the observed and estimated wavefields for a sample shot at the end of the inversion (25 iterations). There is little difference between them, indicating the good performance of the inversion algorithm.

Shown in Fig. 5b is the velocity profile for the final inverted results. The existence of the deep void (blue zone) is indicated underneath the high velocity zone (Vs > 700 m/s) located at the center of the medium.

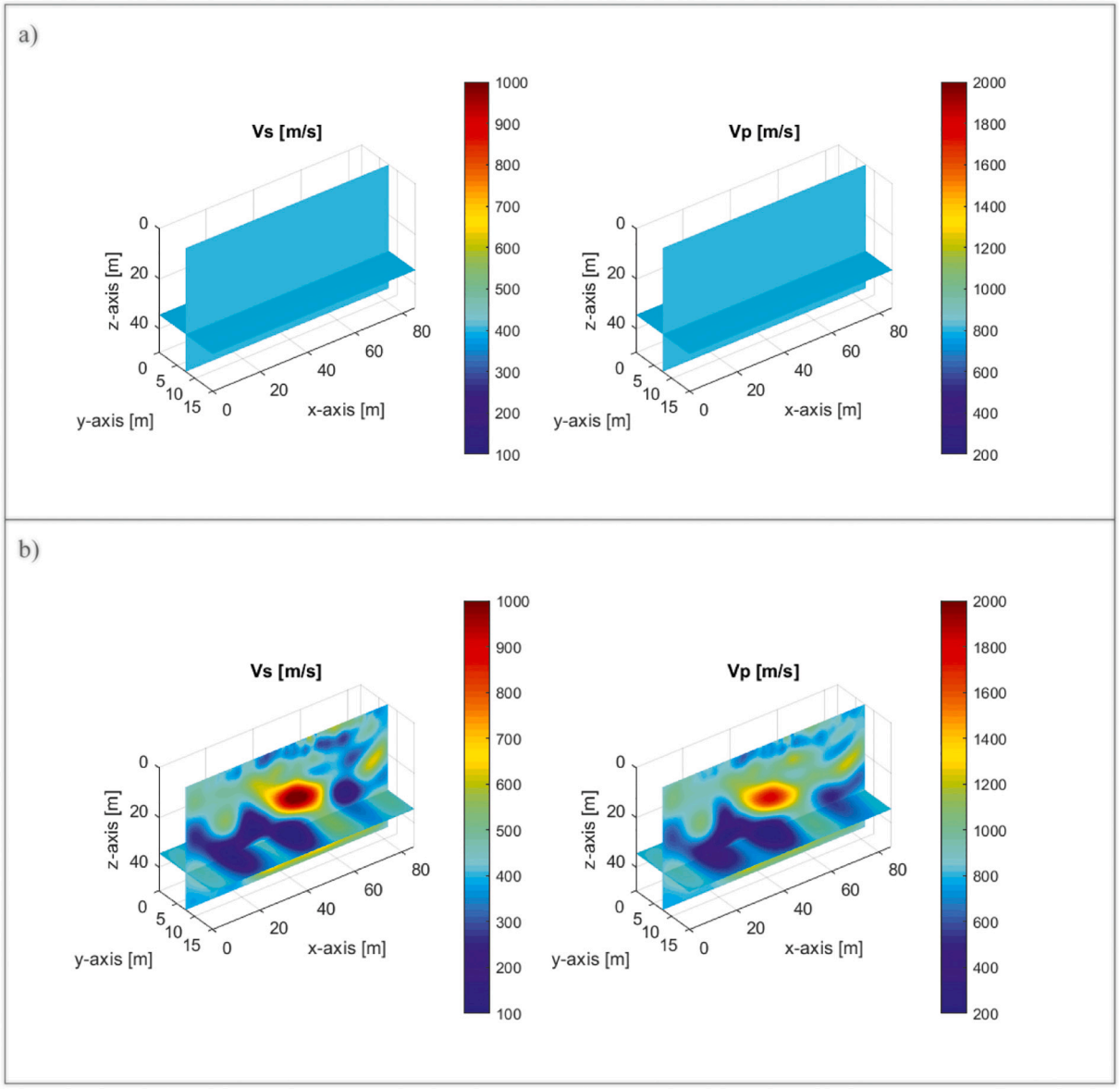

Fig. 5. Field experiment (surface source): a) distribution of Vs and Vp for the initial velocity model used at the beginning of the analysis; b) distribution of Vs and Vp for the final inverted result at the end of the 5–25 Hz frequency stage.

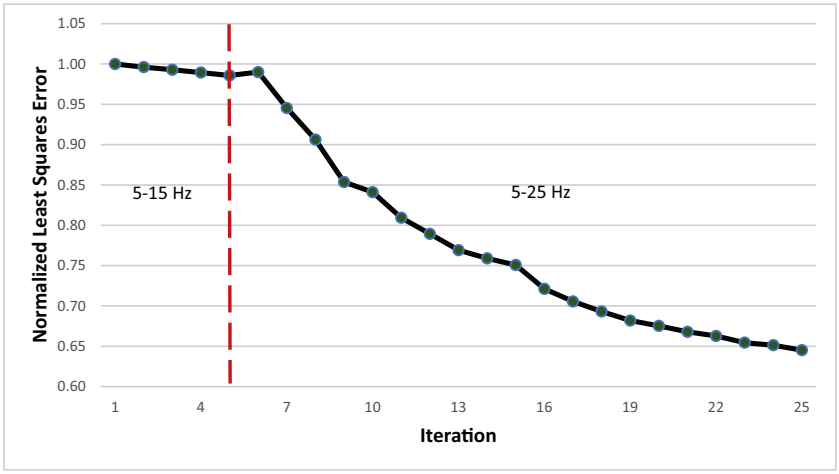

Fig. 6. Field experiment (surface source): Normalized least-squares error for the entire inversion run.

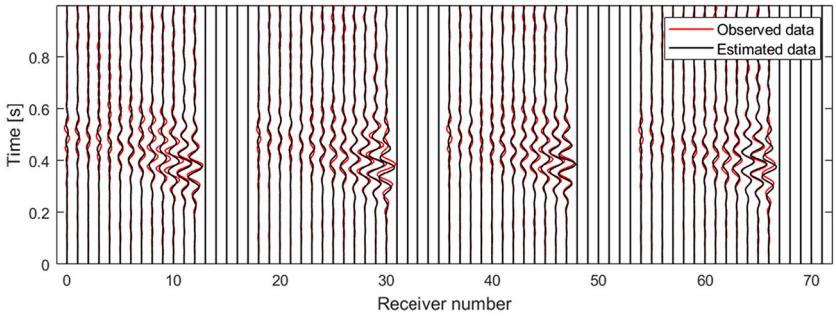

Fig. 7. Field experiment (surface source): wavefield comparison for a sample shot at the end of inversion.

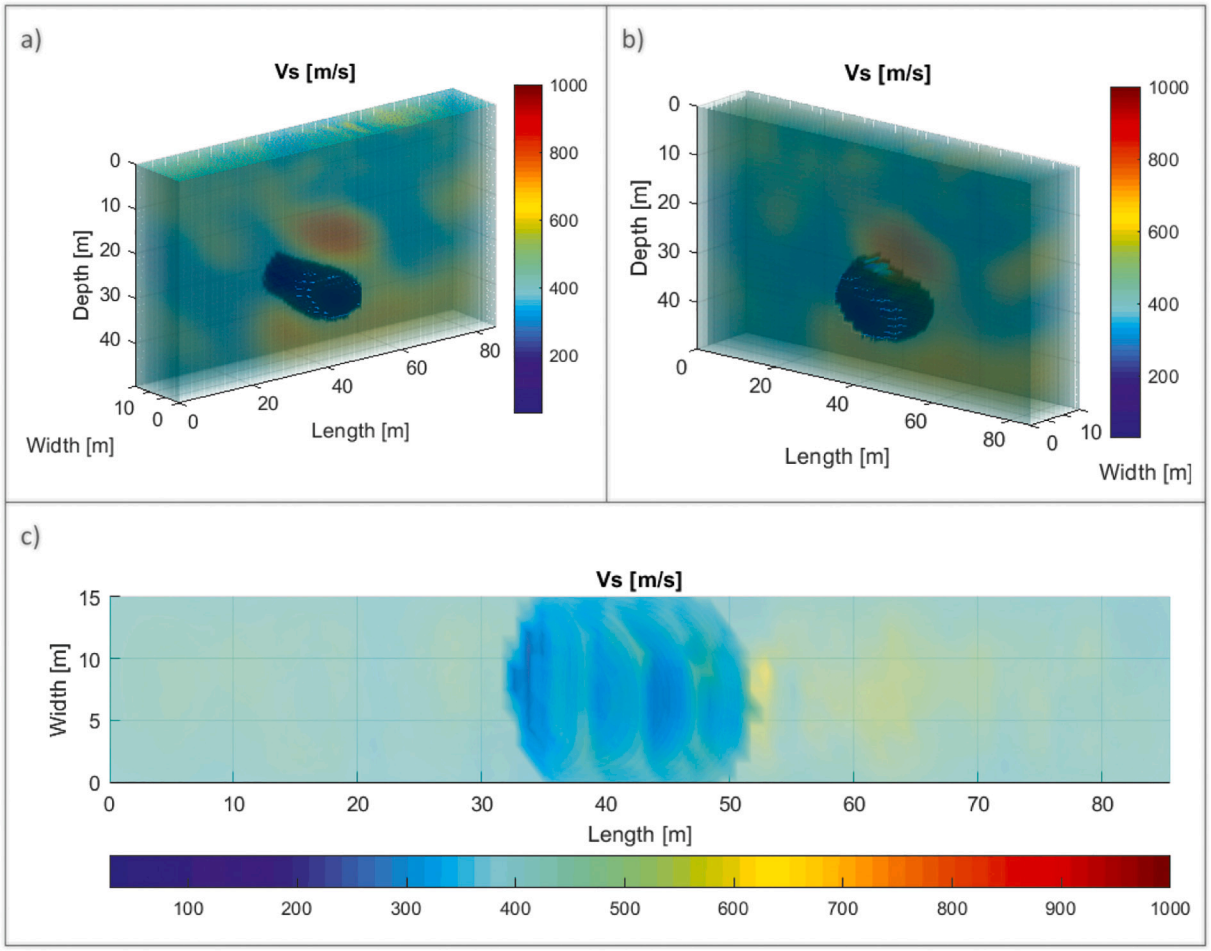

Fig. 8. Field experiemnt (surface source): 3D rendering of the final inverted result at two different viewing angles (a, b) and the top-down view (c). The rendering was generated by passing multiple transects at each grid point and setting the value of the pixels above 250 m/s to become transparent.

There are some indications of another low velocity zone connected to the deep void. This most likely represents zones of soft material around the void. Shown in Fig. 8 is a 3D rendering of the final inverted results at two different view angles, and the top-down view of the void. These renderings were generated by passing 2D slices through the velocity profile at different locations in the 3D space and setting a cutoff velocity value, above which the medium becomes transparent. This way we were able to focus on the void and reveal its features. Note that the inverted Vs is 50 to 150 m/s near the void center, and we added 100 m/s (transition zone) to the range to have the cutoff value of 250 m/s to capture the void boundary.

The interpreted lateral extent of the void spans the entire test area in the north-south direction, to the outer edges of the analyzed domain. There is also an indication of a localized high velocity zone on top of the void, which is made transparent in the rendering. This high velocity zone was consistent with the SPT boring profile and was determined from the boring log to be mostly made up of fossiliferous limestone with some sand.

To verify the seismic results, borehole sonar testing was also performed at the test site by an independent contractor (Universal Engineering). For sonar testing, the Imagenex Sonar Model 881A was used. It operates at tunable frequencies from 600 kHz to 1 MHz in 5 kHz steps and range scales of 1 m to 100 m with resolution from 2 mm to 10 mm. An in-house processing software was used by the contractor for processing of sonar data. Shown in Fig. 9 is the overlay of the interpreted void location using the top-down view of the rendering results (Fig. 8c)

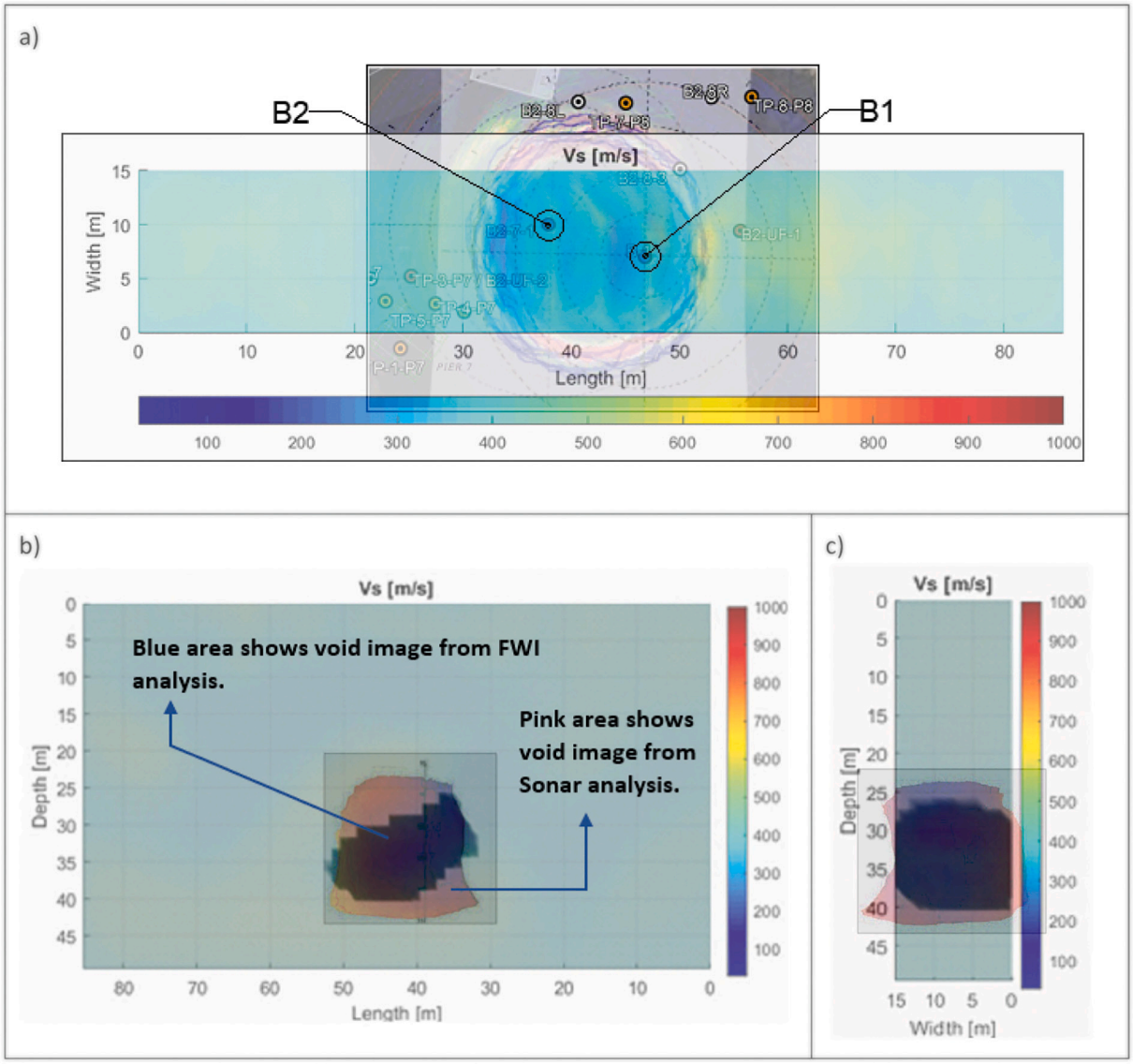

Fig. 9. Field experiment (surface source): a) overlay of the final inverted result and void location from sonar analysis. B1 and B2 locations are used to draw SPT comparison plots in Fig. 10; b) side view overlay of the inverted and sonar imaging in the north-south direction facing south; c) side view overlay of the inverted and sonar imaging in the east-west direction facing east.

and the result of the sonar analysis (Fig. 9a), along with side overlays of the void in the north-south and east-west directions (Fig. 9b, c). A good overall match of the void extents is achieved. The sonar image extends beyond the north-south boundaries of the inverted zone. Overall, the void is measured at about 20 m in lateral diameter, consistent with the sonar image. Vertical side view of the void in the north-south direction facing south (Fig. 9b) shows the void depth for the inverted results from 25 m at its shallowest to 40 m at its deepest. Vertical side view of the void in the east-west direction facing east shows its lateral extents to beyond the analyzed domain. There is some disagreement in the vertical void dimensions between the inverted and sonar results in the north-south overlay (Fig. 9b). This is due to the limited signal coverage and ray paths along the narrow width from the surface sources.

Shown in Fig. 10 is the comparison of the SPT blow counts (N) and the final velocity profile for Vs at two locations shown in Fig. 9a. Overall, there is good agreement between the profiles, verifying the existence of the void and the high-velocity zone above. The SPT results are more erratic than the inverted velocity results. This is due to the higher sensitivity of the SPT test to local variations of material properties compared to the seismic FWI method. Also, the FWI method produced Vs values for $1.5 \times 1.125 \times 1.5$ m^3 cells, while the SPT samples N values were at 0.3 m intervals. In addition, the regularization (Eq. 2) approach, i.e. adding more weight to the diagonal elements of the Hessian matrix and constraining adjacent cells together during the inversion process will result in some smoothing of the velocity profiles.

4. Deep source (SPT seismic)

4.1. Test configuration and field testing

Deep source testing with the SPT-seismic approach (Mirzanejad et al., 2020b) was also carried out at the same test site. An automatic hammer SPT rig was used to carry out two SPTs, southwest and northeast of the deep void location. Shown in Fig. 11 is the same testing configuration used for the surface-based tests (72 geophones located in a 4×18 grid of 3 m $\times$ 4.5 m spacing) and two vertical source lines to a depth of 52.5 m. SPT sampling occurred at 1.5 m intervals, with additional blows over the final 0.3 m of each interval for seismic testing. Signals were recorded at all 72 geophones for each blow and summed (stacked) to reduce unwanted ambient noise (e.g., vehicles passing) in

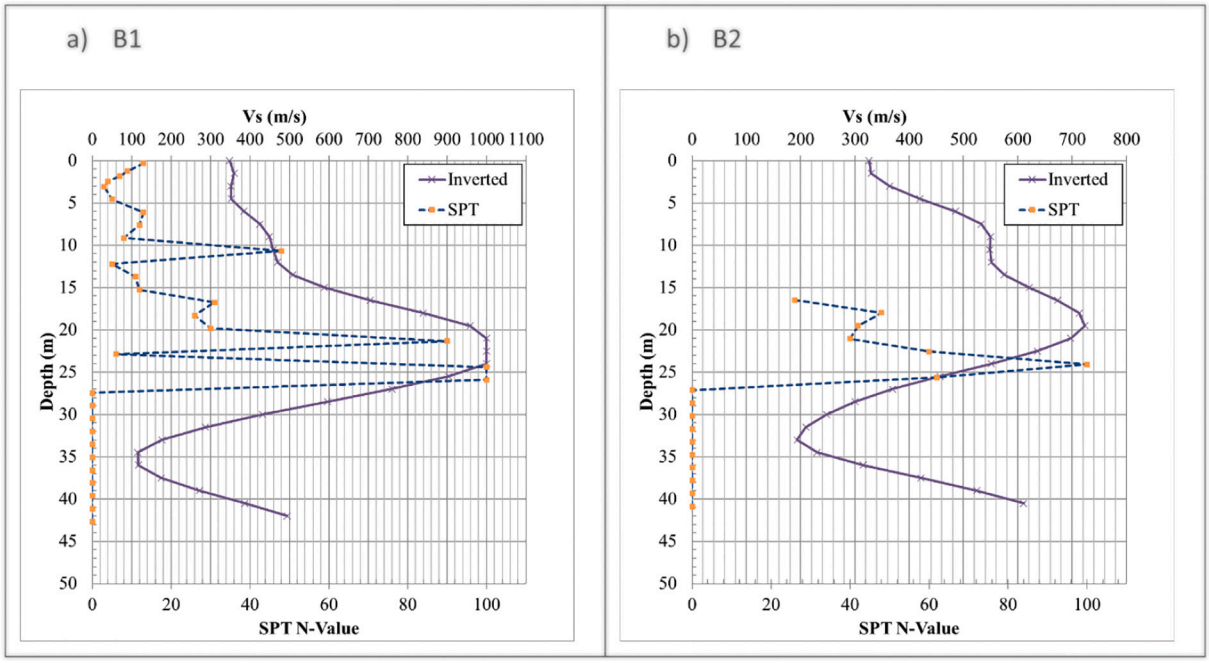

Fig. 10. Field experiment (surface source): comparison of FWI result and N values at two SPT locations (B1 and B2) shown in Fig. 9a.

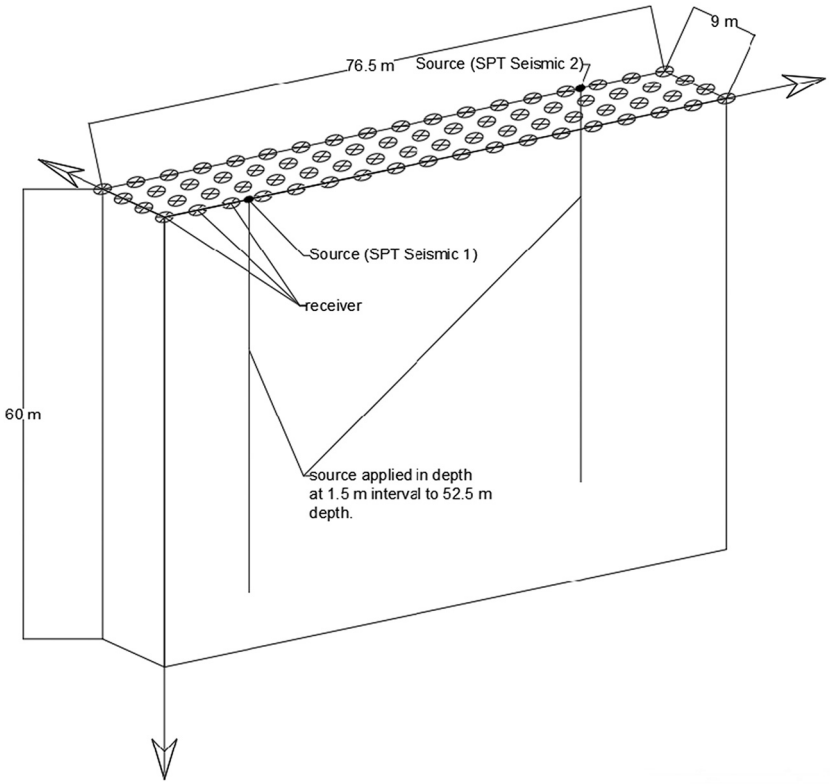

Fig. 11. Testing configuration for SPT-seismic experiment.

the data during the analysis. In total 70 different SPT depths (35 from each SPT borehole) extending from the surface to depth of 52.5 m were recorded for the analysis. Compared to the surface source, the SPT source produced more energy at higher frequencies (25 to 35 Hz). The recorded data with consistent wave magnitudes and phases were in the range of 5–55 Hz, which were used for analysis.

4.2. Analysis and results

The analyzed medium was 60 m × 85.5 m × 15 m (depth × length × width). Again, the medium size was chosen to be larger than the testing configuration shown in Fig. 11, to capture void features that lie outside of the testing zone. A homogeneous initial velocity model (Fig. 12a) was chosen to initiate the inversion process based on the spectral analysis

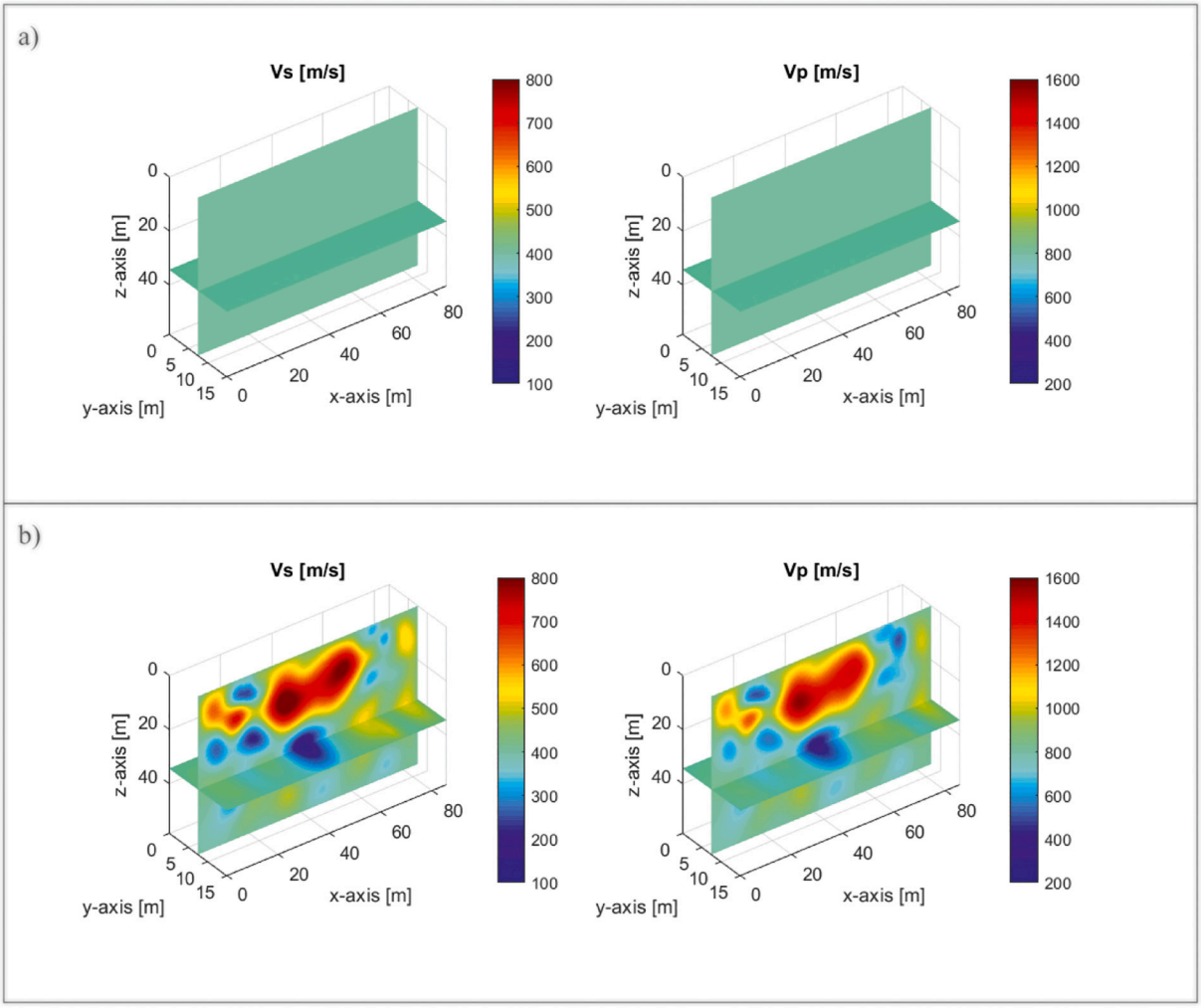

Fig. 12. SPT-seismic experiment: a) distribution of Vs and Vp for the initial velocity model used at the beginning of the analysis; b) distribution of Vs and Vp for the final inverted result at the end of the 5–35 Hz frequency stage.

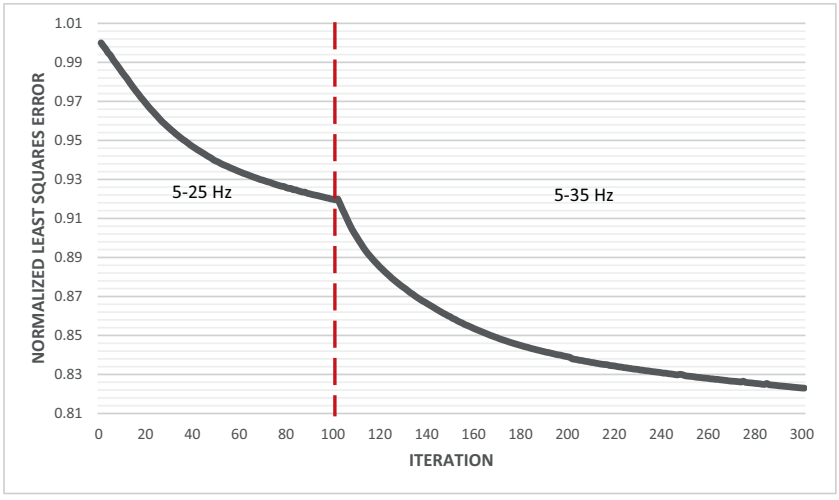

Fig. 13. SPT-seismic experiment: normalized least-squares error for the entire inversion run.

method.

The inversion process began on the field data filtered at 5–25 Hz with the center frequency of 17 Hz for the first stage, using the initial model shown in Fig. 12a. The implemented Gauss-Newton optimization algorithm successfully approached the global minimum and the error decreased to a normalized value of 0.92 at the end of the predefined 100 iterations (Fig. 13). It is noted that waveform data of the SPT-seismic testing is more complex than that of the surface-based testing due to

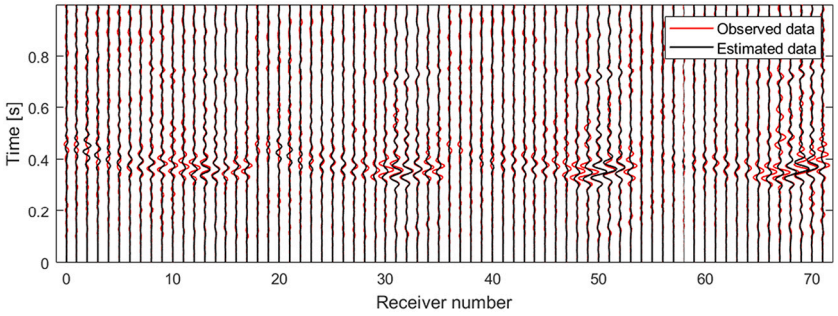

Fig. 14. SPT-seismic experiment: wavefield comparison for a sample shot at the end of inversion.

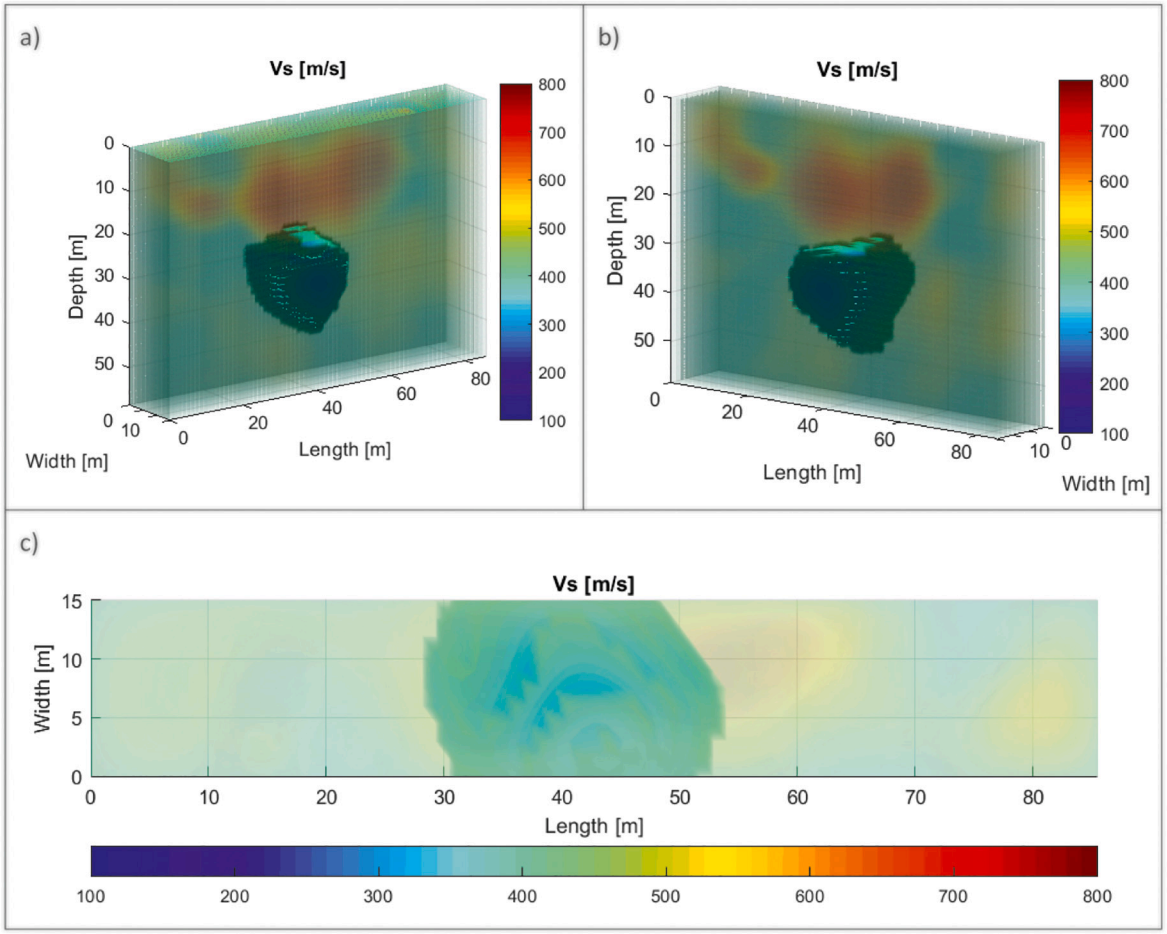

Fig. 15. SPT-seismic experiment: 3D rendering of the final inverted result at two different viewing angles (a, b) and the top-down view (c). The rendering was generated by passing multiple transects at each grid point and setting the value of the pixels above 350 m/s to become **transparent.**

the addition of diffraction/transmission effects. Therefore, more iterations are required to reach convergence.

The field data was then filtered through a 5–35 Hz window with the central frequency of 25 Hz, and used in the second stage with the results of the velocity profile from the first stage as input model. The error further decreased to 0.82 at the end of the inversion process (300 iterations). Shown in Fig. 14 is the waveform comparison the observed (field) data and estimated data associated with the final inverted result for a sample shot. Overall, the phase and amplitude match well for most channels. There is still some discrepancy between the observed and estimated waveforms. This can be attributed to noises that still remained in the observed data after conditioning, which cannot be described through the forward simulation to compute the estimated data.

Shown in Fig. 12b is the final inverted result after 300 iterations for Vs and Vp profiles. There is an indication of a large void (blue zone) at the center. The void is overlain by a large high-velocity zone (Vs > 700 m/s) closer to the surface. Unlike to the surface-based analysis, the inverted Vs of SPT-source data is 150 to 250 m/s near the void center. Again, we added 100 m/s (transition zone) to the range to have the cutoff value of 350 m/s to capture the void boundary. Shown in Fig. 15a to 15c are the 3D renderings of the final inverted result at two different viewing angles as well as the top-down view, respectively. The interpreted extent of the void spans the entire testing area laterally to outside of the analysis region. There is indication of a high-velocity zone on top

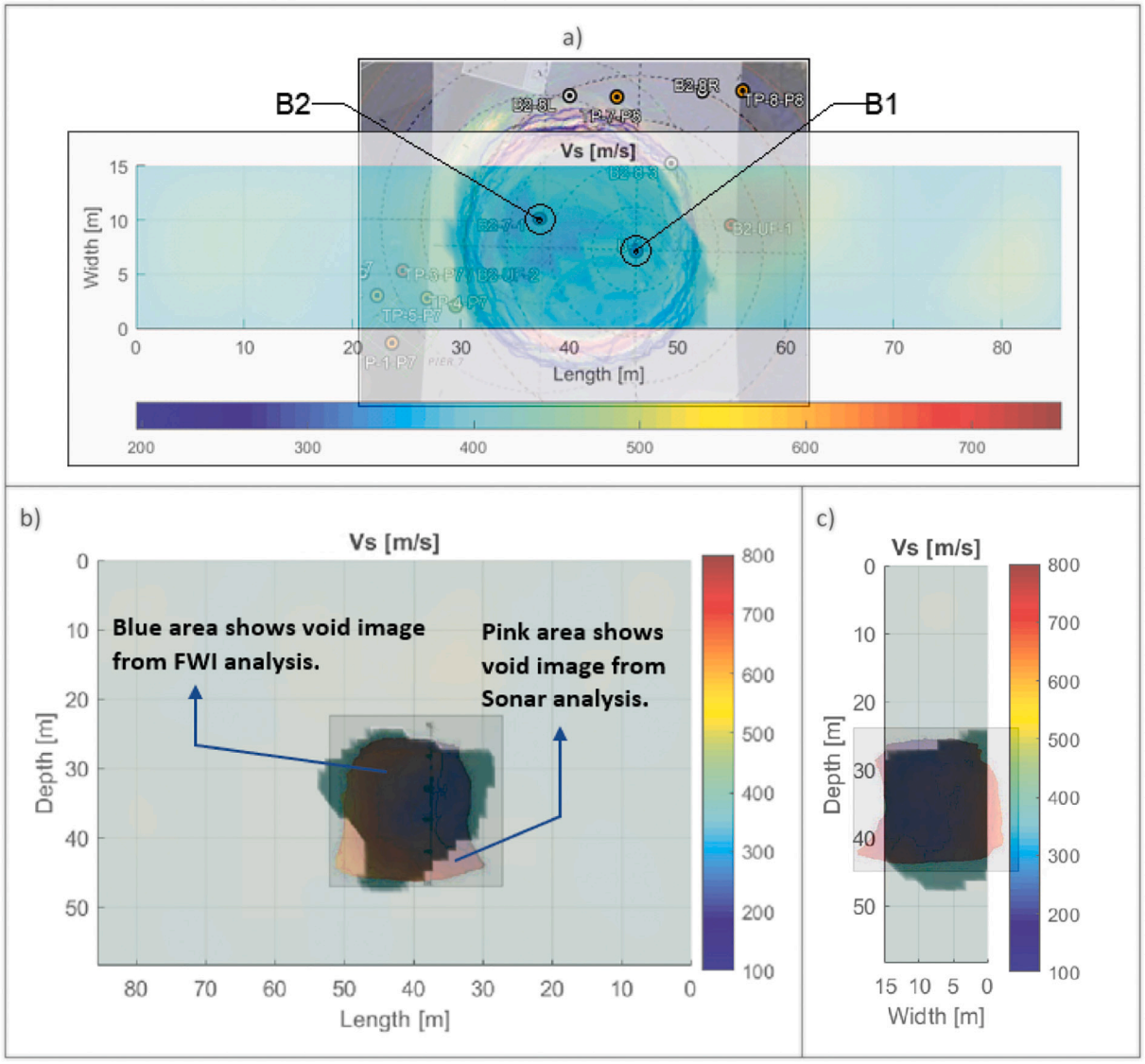

Fig. 16. SPT-seismic experiment: a) overlay of the FWI result and sonar imaging. B-1 and B2 are SPT locations for comparison shown in Fig. 17; b) side view overlay of the inverted result and sonar imaging in the north-south direction facing south; c) side view overlay of the inverted result and sonar imaging in the east-west direction facing east.

of the void and a low-velocity zone to the left (west). Overall, the features are similar to those of the surface-based testing (Fig. 8) in type and relative positions.

Shown in Fig. 16a is the top-down overlay of the FWI and sonar results. The void is matched relatively well at the center, and both results show lateral extension to outside of the testing zone. Shown in Fig. 16b and c is the side overlay comparison of the FWI and sonar images in the north-south direction and the east-west direction, respectively. There is good agreement between the two results in all directions. The extent of the void is from about 25 m to 45 m depth, with a vertical dimension of about 20 m. Compared to the surface-based result (Fig. 9b), the SPT-seismic result (Fig. 16b) is more consistent with the sonar image.

Fig. 17 shows the SPT N-value comparisons with the shear wave velocity, Vs, of the final inverted result at the two locations shown in Fig. 16. The interpreted position of the void in depth is confirmed by SPT borings B1 and B2 (initial borings that identified void). The high velocity zone is also verified, however, its depth is not as good as that observed in the surface-based testing (Fig. 10). This can be attributed to two reasons: 1) the location of the SPT spoon at each source depth (spoon is driven 0.3 m), which can be slightly different than the source position assumed during the analysis, and 2) the signal coverage of SPT-seismic wavefields at shallow depths is less than that of the surface-based wavefields (more sources at the surface).

5. Discussions

Sinkholes as shown in this study and other relative research (Gómez-Ortiz and Martín-Crespo, 2012; Song et al., 2012; Nam and Shamet, 2020) are a major cause for concern in civil engineering projects across the globe. This is due to a lack of certainty regarding the existence of these geological features at the construction site and the difficulty of remediation process. In most cases, the detection of sinkholes occurs when there is visible damage to the structure. At this stage, it is usually too late and costly for remediation and reconstruction efforts to take place.

The detection of deep underground voids as put forth in this research requires tremendous effort if using invasive testing methods, mainly due to the need for physically intersecting the void at such depths. Geophysical methods as shown here are a viable option due to their ease of implementation in the field and high imaging resolution. Amongst

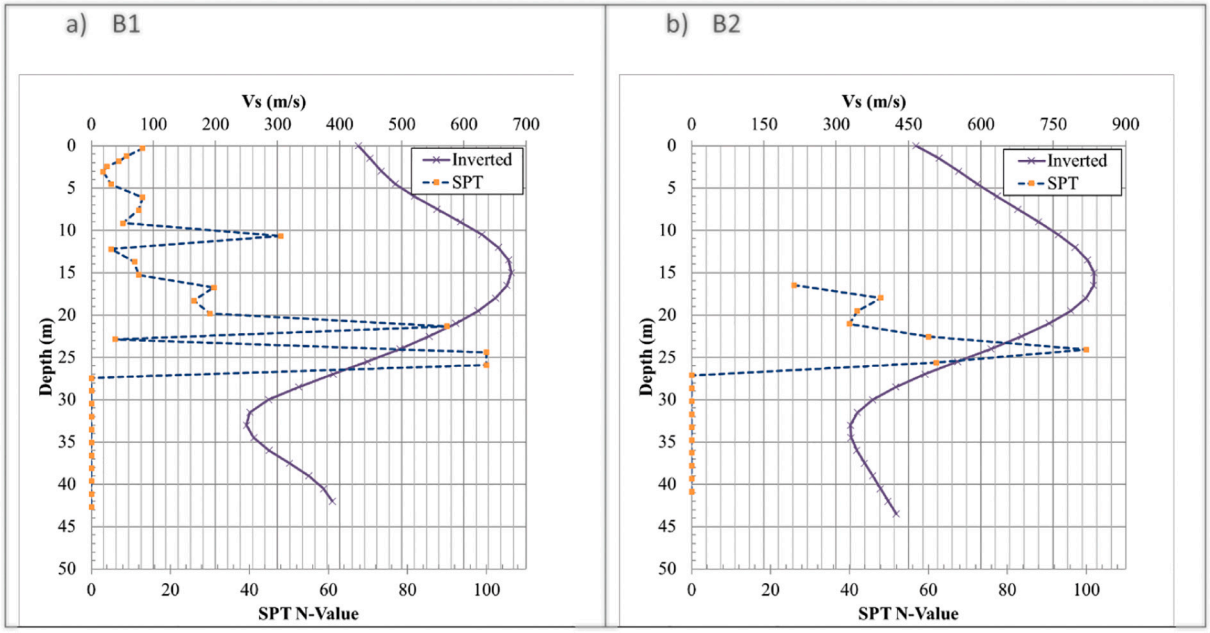

Fig. 17. SPT-seismic experiment: comparison of the inverted Vs and SPT results at two locations shown in Fig. 17a.

common geophysical methods (e.g., ERT, GPR), seismic imaging has the advantage of striking a balance between resolution and detection depth. Nonetheless, using source and receivers on the ground surface has been shown (Mirzanejad et al., 2020b) to have its limitations in terms of the void detection depth. This is mostly due to the greater attenuation of high frequency components of the propagating seismic waves along with other factors that were previously mentioned.

Common surface-based sources (i.e., sledgehammer) are unable to generate enough energy at low frequencies (<10 Hz). The higher frequency components generated by such surface sources must travel down to the desired detection depth and be reflected from any underlying deep anomalies. This extra path of travel effectively reduces the energy of the high frequency component of the reflected waves, thereby making detection of underlying deep voids extremely difficult. Using surface sources capable of generating more energy at lower frequencies (down to 5 Hz) can alleviate this issue, and allows for greater detection depths using surface-based testing.

Alternatively, sending the source into the ground reduces the travel path of the propagating waves. This makes the detection of void signatures on the ground surface more feasible even at higher frequencies. It can be seen from the frequency range considered (Figs. 6 and 13), that higher frequencies of 5–35 Hz were used in the current study for deep void detection using the SPT source compared to the 5–25 Hz range used in the surface source. Another advantage of sending the source into the ground is that more information can be recorded on the surface, due to wider range of wave interaction phenomena with the underlaying structures. The dominant modes of wave interaction in a surface-based testing (both source and geophones on the surface) is through reflection and refraction. Using in-depth SPT source testing with geophones on the surface allows for transmission and diffraction phenomena to also contribute to the inversion process.

On the downside, this added information in the SPT source requires more effort in terms of the optimization demand. As shown in Figs. 13, 300 iterations were required to achieve convergence in the SPT source results. This is in clear contrast to the 25 iterations that were required in the surface-based results shown in Fig. 6. The surface-based source was able to achieve lower velocity values (V_s~50−150 m/s) than those from SPT source (V_s~150−250 m/s) at the void location. This difference is due to the local nature of the gradient-based optimization process used in the current study, and the variations in the acquired field data between the two test types. Nonetheless, comparing results from Fig. 9b and c to Fig. 16b and c, it is observed that the SPT source provides a better match with the overall shape of the void as determined by the sonar analysis. The better match of the SPT source to the sonar survey is also evident from Table 1, where the void volume is shown for results of the sonar survey, surface-based (Fig. 8), and SPT source (Fig. 15). It is observed that void volume from the Sonar survey is measured at 3404 m^3, while that of the SPT source and the surface source are 3888 m^3 and 2607 m^3, respectively.

Table 1
Comparison of void volume measured by two source types and sonar survey.

Survey Type	Void volume (m^3)
Sonar	3404
SPT Source	3888
Surface Source	2607

6. Conclusions

The application of two different source types for deep void detection was studied using a 3D Gauss-Newton FWI method. A surface-based drop weight and a traditional SPT source were used at a site containing a deep void (25–45 m depth) in limestone. It was observed that both source types performed well with the 3D Gauss-Newton FWI method. The deep void was detected, well characterized, and the lateral dimensions agreed with the sonar imaging profile. SPT-N values generally agreed with the S-wave velocity profile, characterizing the low- and high-velocity zones with good accuracy. The ability to detect voids and anomalies outside of the SPT testing zone and in the earlier stages of the field investigations (first or second SPT boreholes) will determine both the need and the location of subsequent SPT locations, which can greatly reduce the uncertainty in the project design phase. The SPT-seismic test allows the assessment of anomalies and layering, for a large volumetric extent (e.g., 20 m around each SPT to the depth of SPT borehole). Finally, the paper reveals that the 3D GN-FWI is a viable method to detect deep voids, provided the right equipment is used to gather data.

Declaration of Competing Interest

None

Acknowledgements

This study was financially supported by the Florida Department of Transportation (FDOT): grant BDV31-977-82 and the National Science Foundation: grant CMMI-1930697. The supports are greatly appreciated. The authors would like to thank the Universal Engineering for providing access to the test site and conducting the SPT and borehole sonar data.

References

Fathi, A., Poursartip, B., Stokoe II, K.H., Kallivokas, L.F., 2016. Three-dimensional P-and S-wave velocity profiling of geotechnical sites using full-waveform inversion driven by field data. Soil Dyn. Earthq. Eng. 87, 63–81. https://doi.org/10.1016/j.soildyn.2016.04.010.

Gómez-Ortiz, D., Martín-Crespo, T., 2012. Assessing the risk of subsidence of a sinkhole collapse using ground penetrating radar and electrical resistivity tomography. Eng. Geol. 149, 1–12.

Groos, L., Schäfer, M., Forbriger, T., Bohlen, T., 2017. Application of a complete workflow for 2D elastic full-waveform inversion to recorded shallow-seismic Rayleigh waves. Geophysics 82 (2), R109–R117.

Gutiérrez, F., 2016. Sinkhole hazards. In: Oxford Research Encyclopedia of Natural Hazard Science.

Ivanov, J., Miller, R.D., Feigenbaum, D.Z., Peterie, S.L., 2017. Detecting subsurface objects and identifying voids possibilities using the backscatter analysis of surface wave (BASW) method. In: International Conference on Engineering Geophysics, Al Ain, United Arab Emirates, 9-12 October 2017. Society of Exploration Geophysicists, pp. 116–119.

Jordanov, V.T., Knoll, G.F., 1994. Digital synthesis of pulse shapes in real time for high resolution radiation spectroscopy. Nucl. Inst. Methods Phys. Res. Section A 345 (2), 337–345.

Kiernan, M., Jackson, D., Montgomery, J., McDonald, B., Anderson, J.B., Davis, K.C., 2021. Characterization of a karst site using electrical resistivity tomography and seismic full waveform inversion. J. Environ. Eng. Geophys. https://doi.org/10.32389/JEEG20-045.

Köhn, D., Wilken, D., De Nil, D., Wunderlich, T., Rabbel, W., Werther, L., Schmidt, J., Zielhofer, C., Linzen, S., 2019. Comparison of time-domain SH waveform inversion strategies based on sequential low and bandpass filtered data for improved resolution in near-surface prospecting. J. Appl. Geophys. 160, 69–83.

Manda, A.K., Gross, M.R., 2006. Identifying and characterizing solution conduits in karst aquifers through geospatial (GIS) analysis of porosity from borehole imagery: an example from the Biscayne aquifer, South Florida (USA). Adv. Water Resour. 29 (3), 383–396.

Mecking, R., Köhn, D., Meinecke, M., Rabbel, W., 2021. Cavity detection by SH-wave full-waveform inversion—a reflection-focused approach. Geophysics 86 (3), WA123–WA137.

Mirzanejad, M., Tran, K.T., 2019. 3D viscoelastic full waveform inversion of seismic waves for geotechnical site investigation. Soil Dyn. Earthq. Eng. 122, 67–78. https://doi.org/10.1016/j.soildyn.2019.04.005.

Mirzanejad, M., Tran, K.T., McVay, M., Horhota, D., Wasman, S., 2020a. Sinkhole detection with 3D full seismic waveform tomography. Geophysics 85 (5), B147–B157.

Mirzanejad, M., Tran, K.T., McVay, M., Horhota, D., Wasman, S., 2020b. Coupling of SPT and 3D full waveform inversion for deep site characterization. Soil Dyn. Earthq. Eng. 136, 106196. https://doi.org/10.1016/j.soildyn.2020.106196.

Nam, B.H., Shamet, R., 2020. A preliminary sinkhole raveling chart. Eng. Geol. 268, 105513.

Nasseri-Moghaddam, A., Cascante, G., Hutchinson, J., 2005. A new quantitative procedure to determine the location and embedment depth of a void using surface waves. J. Environ. Eng. Geophys. 10 (1), 51–64.

Nasseri-Moghaddam, A., Cascante, G., Phillips, C., Hutchinson, D.J., 2007. Effects of underground cavities on Rayleigh waves—Field and numerical experiments. Soil Dyn. Earthq. Eng. 27 (4), 300–313.

Nguyen, T.D., Tran, K.T., 2018. Site characterization with 3D elastic full-waveform tomography. Geophysics 83 (5), R389–R400. https://doi.org/10.1190/geo2017-0571.1.

Park, C.B., Miller, R.D., Xia, J., 1999. Multichannel analysis of surface waves. Geophysics 64 (3), 800–808.

Plessix, R.E., Michelet, S., Rynja, H., Kuehl, H., Perkins, C., de Maag, J.W., Hatchell, P., 2010, June. Some 3D applications of full waveform inversion. In: 72nd EAGE Conference and Exhibition-Workshops and Fieldtrips (pp. cp-162). European Association of Geoscientists & Engineers.

Prada, J., Fratta, D., Santamarina, J.C., 2000. Tomographic detection of low-velocity anomalies with limited data sets (velocity and attenuation). Geotech. Test. J. 23 (4), 472–486.

Putnam, N.H., Peng, X., Cawlfield, J.D., Kovin, O.N., Torgashov, E.V., Modur, P., Stagner, C., Grant, S.L., Anderson, N.L., Nasseri-Moghaddam, A., 2009, January. Attenuation analysis of Rayleigh waves used to locate shallow manmade tunnels. In: In 43rd US Rock Mechanics Symposium & 4th US-Canada Rock Mechanics Symposium. American Rock Mechanics Association.

Romdhane, A., Grandjean, G., Brossier, R., Réjiba, F., Operto, S., Virieux, J., 2011. Shallow-structure characterization by 2D elastic full-waveform inversion. Geophysics 76 (3), R81–R93.

Sloan, S.D., 2017. Role of depth in anomaly detection using near-surface seismic methods. In: International Conference on Engineering Geophysics, Al Ain, United Arab Emirates, 9-12 October 2017. Society of Exploration Geophysicists, pp. 132–135.

Sloan, S.D., McKenna, J.R., Broadfoot, S.W., Metheny, O.M., Peterie, S.L., Miller, R.D., Ivanov, J., 2012, November. Tunnel detection using near-surface seismic methods. In: 2012 SEG Annual Meeting. Society of Exploration Geophysicists.

Smith, J.A., Borisov, D., Cudney, H., Miller, R.D., Modrak, R., Moran, M., Peterie, S.L., Sloan, S.D., Tromp, J., Wang, Y., 2019. Tunnel detection at Yuma Proving Ground, Arizona, USA—Part 2: 3D full-waveform inversion experiments. Geophysics 84 (1), B95–B108.

Song, K.I., Cho, G.C., Chang, S.B., 2012. Identification, remediation, and analysis of karst sinkholes in the longest railroad tunnel in South Korea. Eng. Geol. 135, 92–105.

Tran, K.T., Luke, B., 2017. Full waveform tomography to resolve desert alluvium. Soil Dyn. Earthq. Eng. 99, 1–8. https://doi.org/10.1016/j.soildyn.2017.04.018.

Tran, K.T., McVay, M., Faraone, M., Horhota, D., 2013. Sinkhole detection using 2D full seismic waveform tomography. Geophysics **78** (5), R175–R183. https://doi.org/10.1190/geo2013-0063.1.

Tran, K.T., Mirzanejad, M., McVay, M., Horhota, D., 2019. 3-D time-domain Gauss–Newton full waveform inversion for near-surface site characterization. Geophys. J. Int. 217, 206–218. https://doi.org/10.1093/gji/ggz020.

Vireux, J., Operto, S., 2009. An overview of full-waveform inversion in exploration geophysics. Geophysics **74** (6), WCC1–WCC26. https://doi.org/10.1190/1.3238367.

Wang, Y., Miller, R.D., Peterie, S.L., Sloan, S.D., Moran, M.L., Cudney, H.H., Smith, J.A., Borisov, D., Modrak, R., Tromp, J., 2019. Tunnel detection at Yuma Proving Ground, Arizona, USA—Part 1: 2D full-waveform inversion experiment. Geophysics 84 (1), B95–B105.

Warner, M., Ratcliffe, A., Nangoo, T., Morgan, J., Umpleby, A., Shah, N., Vinje, V., Štekl, I., Guasch, L., Win, C., Conroy, G., 2013. Anisotropic 3D full-waveform inversion. Geophysics 78 (2), R59–R80.